Chapter 1

Dual-Mass MEMS Gyroscope Structure, Design, and Electrostatic Compensation

Huiliang Cao and Jianhua Li

Additional information is available at the end of the chapter

http://dx.doi.org/10.5772/intechopen.74364

Abstract

Dual-mass MEMS gyroscope is one of the most popular inertial sensors. In this chapter, the structure design and electrostatic compensation technology for dual-mass MEMS gyroscope is introduced. Firstly, a classical dual-mass MEMS gyroscope structure is proposed, how it works as a tuning fork (drive anti-phase mode), and the structure dynamical model together with the monitoring system are presented. Secondly, the imperfect elements during the structure manufacture process are analyzed, and the quadrature error coupling stiffness model for dual-mass structure is proposed. After that, the quadrature error correction system based on coupling stiffness electrostatic compensation method is designed and evaluated. Thirdly, the dual-mass structure sensing mode modal is proposed, and the force rebalancing combs stimulation method is utilized to achieve sensing mode transform function precisely. The bandwidth of sensing open loop is calculated and experimentally proved as 0.54 times with the resonant frequency difference between sensing and drive modes. Then, proportional-integral-phase-leading controller is presented in sensing close loop to expand the bandwidth, and the experiment shows that the bandwidth is improved from 13 to 104 Hz. Finally, the results are concluded and summarized.

Keywords: MEMS gyroscope, dual-mass structure, mode analysis, quadrature error, bandwidth expansion, electrostatic compensation

1. Introduction

The precision of micro-electro-mechanical system (MEMS) gyroscope improves a lot in this decade, and achieves the tactical grade level. On the benefits of the small size, low costs, and light weight the MEMS gyro is applied in more and more areas, such as inertial navigation, roller detection, automotive safety, industrial controlling, railway siding detection, consumer

electronics and stability controlling system [1–5]. During use, the acceleration along the sense axis causes great error in MEMS gyroscope output signal, and dual-mass gyroscope structure restrains this phenomenon well by employing differential detection technology; so, a lot of research institutes are interested in this structure [6–8].

1.1. Development of dual-mass MEMS gyroscope structure quadrature error compensation

Most of the literature informs that the dominate signal component in output signal is quadrature error, which is generated in the structure manufacture process, and brings over several $100^\circ\ S^{-1}$ equivalent input angular [9–14]. The original source of quadrature is the coupling stiffness, which is modulated by drive mode movement and generates quadrature error force. The force has same frequency but has a 90° phase difference with Coriolis force and stimulates sense mode [11]. Most previous works utilize phase-sensitivity demodulation method to pick Coriolis signal from sense channel [9, 13], which requires accurate phase information and long-term, full-temperature range stability. However, the demodulation phase error and noise usually exist (sometimes more than 1° [9, 12]), which bring undesirable bias. The coupling stiffness drift (the drive and sense modes' equivalent stiffness vary with temperature and generate the drift of coupling stiffness [6, 11]) causes the quadrature error force drift, which is considered to be one of the most important reasons leading to bias long-term drift, and is proved by [11, 14] experimental work.

The previous works provide several effective ways to reduce quadrature error and are concluded into three aspects after the structure is manufactured [9, 11]: the quadrature signal compensation, the quadrature force correction and coupling stiffness correction. In work [9], the quadrature error is reduced by dc voltage based on synchronous demodulation and electrostatic quadrature compensation method, and the sigma-delta technology is employed in ADC and DAC. The research in Ref. [14] also employs coupling stiffness correction method to improve the performance of "butterfly" MEMS gyroscope. The bias stability and scale factor temperature stability enhance from 89°/h and 662 ppm/°C to 17°/h and 231 ppm/°C, respectively, which achieves the correction goal. The quadrature error correction in dual-mass tuning fork MEMS gyro structure is investigated in literature [11], and this work also proves the quadrature stiffness are different in left and right masses. A quadrature error correction closed loop is proposed in the work, and utilizing the coupling stiffness correction method, the masses are corrected separately. The stiffness correction combs utilize unequal gap method with dc voltages [15]. The bias stability improves from 2.06 to 0.64°/h with Allan Deviation analysis method, and the noise characteristic is also optimized [11]. Another coupling stiffness correction work is proposed in literature [7]; in this work, coupling stiffness correction controller uses PI technology, and the quadrature error equivalent input angular rate is measured as 450°/s. The experiment in the work shows that the bias stability and ARW improve from 7.1°/h and 0.36°/√h to 0.91°/h and 0.034°/√h, respectively. In Ref. [16], quadrature signal is compensated based on charge injecting technology in the sense loop, the compensation signal has same frequency, amplitude and anti-phase with quadrature error signal. The quadrature error correction method proposed in literature [8] employs both the quadrature force and stiffness correction methods, the modulation reference signal is generated by PLL technology and the correction loop uses PI regulator; the two masses are controlled

together. A novel quadrature compensation method is proposed in literature [17] based on sigma-delta-modulators (ΣΔM), the quadrature error is detected by utilizing a pure digital pattern recognition algorithm and is compensated by using DC bias voltages, and the system works beyond the full-scale limits of the analog ΣΔM hardware. The quadrature error is compensated by open-loop charge injecting circuit in Ref. [18], the circuit is implemented on application specific integrated circuits (ASIC) and the experimental results show that the quadrature error component is effectively rejected.

1.2. Development of dual-mass MEMS gyroscope bandwidth expansion

High precision MEMS gyros are reported in literatures, and the bias drift parameters are even better than the tactical grade requirement. But the bandwidth performance always restrains the MEMS gyro application (100 Hz bandwidth is required in both Tactical and Inertial Grade) [4]. For most linear vibrating MEMS gyro, the mechanical sensitivity is determined by the difference between drive and sensing modes' resonant frequencies Δf. It means smaller difference achieves higher mechanical sensitivity (such as higher scale factor, higher resolution and smaller output noise) [19]. It is also proved that the mechanical bandwidth of the gyro is about $0.54\Delta f$ [20], so smaller Δf causes worse bandwidth characteristic. Some works employ mode-matching technology to make $\Delta f \approx 0$ Hz, and the best mechanical sensitivity can be acquired but bandwidth is sacrificed. It seems like that the bargain should be made between mechanical sensitivity and bandwidth in sensing open loop. So the sensing closed loop is required to improve MEMS gyro dynamic characteristics and bandwidth. The work in [21] employs a ΣΔ closed loop to reduce the frequency difference between the drive and sensing mode to less than 50 Hz. The research in work [22] utilizes PI controlling technology to make Δf tunable, and the bandwidth is optimized to 50 Hz. The sensing closed loop for single mass MEMS gyroscope based on automatic generation control (AGC) technology is proposed in paper [23]. The force rebalance controller extends the bandwidth, but it only contains a pure integral section which makes sensing closed loop with high Q value structure unstable. The bandwidth for another single mass MEMS gyroscope is introduced in work [24]; the bandwidth is improved from 30 to 98 Hz with notch filter and lead–lag compensator. The notch filter is designed for the "peak response" caused by the conjugate complex poles at Δf. But the resonant frequencies of the drive and sensing modes usually drift with temperature [6], so the notch filter method cannot satisfy the temperature-changing environment. The work in [25] proposes a method to avoid problems caused by notch filter and expands the bandwidth from 2.3 to 94.8 Hz. However, its left and right sensing modes are not coupled, and the bandwidth is only determined by the low pass filter (different with left and right sensing modes coupled structure). Its dual-mass structure can be considered as two independent gyroscopes with different Δfs, and two sensing loops should be designed separately to expand the bandwidth. The left and right sensing modes coupled structures are investigated in [26, 27, 28]. The work in Ref. [26] illustrates the vibration characteristics of dual-mass and spring structure. The work in Ref. [27] analyzes the energy of gyroscope under in-phase and anti-phase modes. And literature [28] proposes that the real working sensing mode of gyroscope is formed by sensing in-phase and anti-phase modes. However, these works do not focus on the bandwidth method of this kind of sensing loop. The gyro bandwidth optimized by mechanical method is proposed in Ref. [29], but the bandwidth varies with the temperature. Literature [30] employs eight drive mode units to

form a drive band (not a single frequency). It provides a high mechanical sensitivity band for the gyroscope, but the bandwidth is determined by sensing mode frequency. And the phase margin of the closed loop is difficult to design. In Ref. [31], the bandwidth estimation methods of MEMS gyroscope in open loop and closed loop are proposed, but the bandwidth expanding method is not discussed clearly. The precise test method of bandwidth is introduced in Ref. [32]. The method uses vibration velocity of virtual drive mode multiplied by virtual angular rate to generate Coriolis force and substitutes angular turntable. The vibration velocity of drive mode is produced by signal source, not by drive mode, which ignores the frequency drift of drive mode and the mechanical coupling between drive and sensing mode.

This chapter focuses on the investigation of the dual-mass MEMS gyroscope structure, and the electrostatic compensation method for the structure, including quadrature error correction and bandwidth expansion technology. Through these technologies, the static and dynamic performance of the MEMS gyroscope is improved.

2. Dual-mass MEMS gyroscope structure design and analysis

2.1. Dual-mass MEMS gyroscope structure design

The fully decoupled linear vibrating gyroscope structure's ideal movement model can be found in many papers; the model can be described as two "spring-mass-damping" systems: drive mode and sense mode. In x-axis direction, drive frame is connected with Coriolis mass which is linked by sense frame in y direction. The drive frame and sense frame can be stimulated by their own mode's effective stiffness and damping, as shown in **Figure 1**. This chapter employs a dual-mass fully decoupled structure as mentioned in [6, 33], and it works in linear vibrating principle, with slide-film combs in both drive and sense modes. The whole

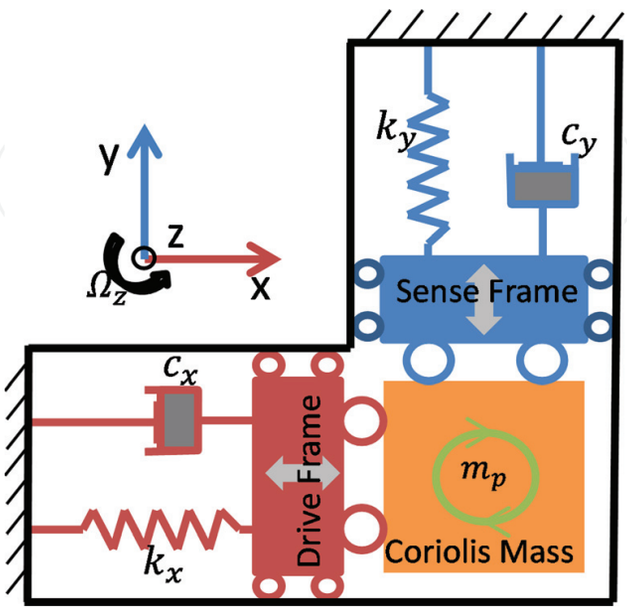

Figure 1. Schematic of ideal gyroscope fully decoupled model.

structure is shown in **Figure 2**. This structure model is constituted by two symmetrical parts, which are connected by two center U-shaped connect springs whose parameters are the same with drive U-shaped spring. The left and right Coriolis mass are sustained by 2 drive U-shaped springs (DS-A,B) and 4 sense U-shaped springs (SS-C,D,E,F), respectively, and these springs are linked by drive and sensing frames. The moving comb fingers are combined with frames while the static ones are fixed with the substrate. The whole structure is suspended and supported by 8 drive (DS-C,D,E,F for left part) and 4 sense (SS-A,B) U-shaped springs [6].

The drive U-shaped springs' stiffness coefficients are large along y-axis and very small in x direction while sense springs have the adverse characteristic. When the structure works, the drive combs support the electrostatic force to stimulate the drive frame and the Coriolis mass (together with SS-C,D,E,F) to move along x direction, and no displacement is generated in sense direction because of SS-A,B. When there is an angular rate Ω_z input around the z-axis, the Coriolis mass together with sense frame and DS-A, B will have a component motion in y orientation under the influence of Coriolis force (the drive frame will not move in y-axis because of the effect of DS-C,D,E,F), and then this displacement involved with Ω_z is detected by the sense combs.

The drive mode of the structure bases on tuning for k theory. The left and right masses are coupled by connect U-shaped spring, when two sensing masses are coupled by the x-axis warp of drive springs. The mode analyses of the first four order modes are shown in **Figure 3** [34]. The first-order mode is drive in-phase mode, the left and right masses together with drive frames vibrate toward same direction along drive axis (x direction in **Figure 2**), as shown in **Figure 3(a)**. The second- and third-order modes are sensing in-phase and anti-phase modes, as shown in **Figure 3(b)** and **(c)**. The left and right masses together with sense frames vibrate in same and inverse directions along sensing axis (y direction in **Figure 2**), respectively. And sensing anti-phase mode is the expected working mode. Drive anti-phase

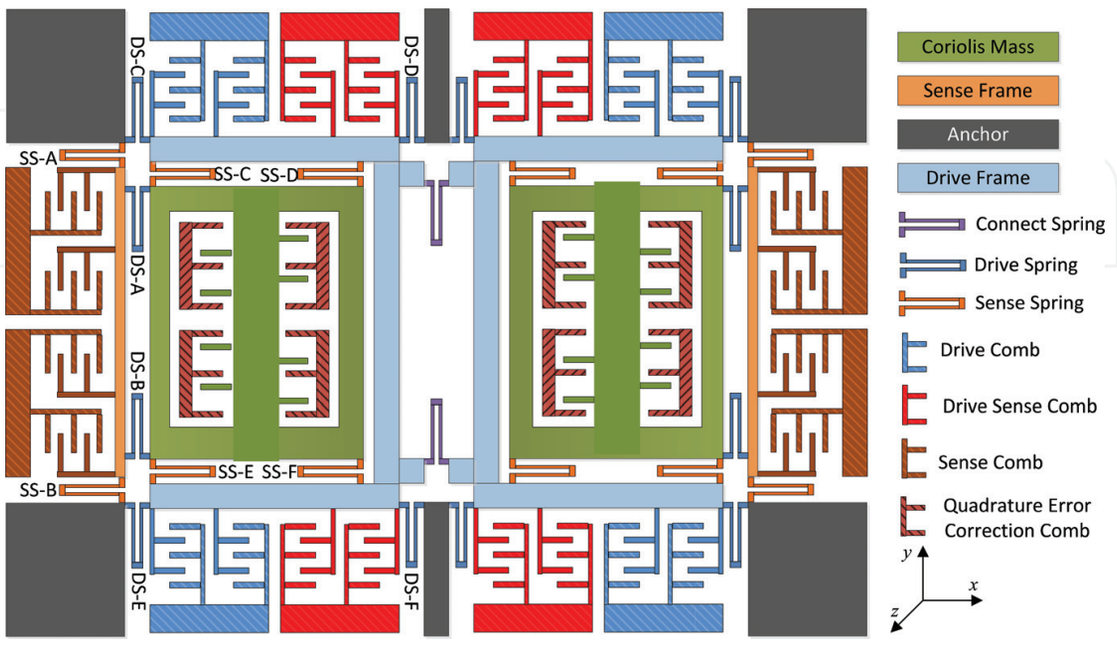

Figure 2. Schematic of the structure.

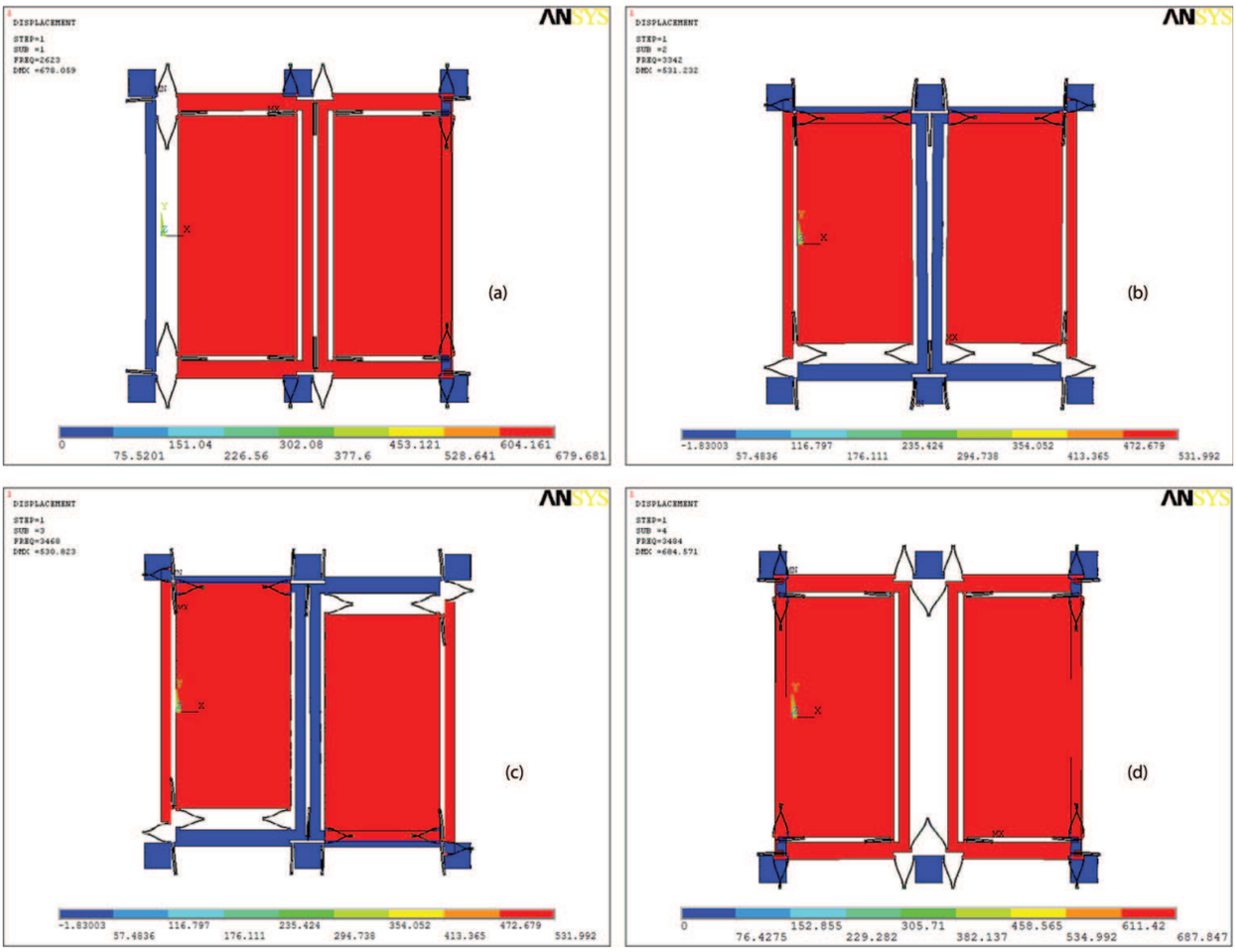

Figure 3. (a) Drive in-phase mode (first mode) with frequency ω_{x1} = 2623 × 2π rad/s; (b) sensing in-phase mode (second mode) with frequency ω_{y1} = 3342 × 2π rad/s; (c) sensing anti-phase mode (third mode) with frequency ω_{y2} = 3468 × 2π rad/s; (d) drive anti-phase mode (fourth mode) with frequency ω_{x2} = 3484 × 2π rad/s.

mode is the fourth order, in which mode, the left and right masses move in inverse directions along drive axis as **Figure 3(d)** shows. The drive anti-phase is another expected working mode.

2.2. Dual-mass MEMS gyroscope structure working principle analysis

Due to a large difference (>1000 Hz) between the in-phase (the first mode) and anti-phase drive modes frequencies, the quality factor of drive anti-phase mode is Q_{x2} > 2000 and the stimulating method of the drive mode. The real working drive mode is considered to be pure anti-phase drive mode (the fourth mode). Considering the real working sensing mode is formed by second and third modes, the motion equation of gyroscope structure can be expressed as (ideal condition) [35]:

$$m\ddot{D} + c\dot{D} + kD = F \tag{1}$$

where $\boldsymbol{m} = \begin{bmatrix} m_x \\ m_y \\ m_y \end{bmatrix}, \boldsymbol{D} = \begin{bmatrix} x \\ y_1 \\ y_2 \end{bmatrix}, \boldsymbol{k} = \begin{bmatrix} k_{xx} & k_{xy1} & k_{xy2} \\ k_{y1x} & k_{y1y1} & 0 \\ k_{y2x} & 0 & k_{y2y2} \end{bmatrix}, \boldsymbol{c} = \begin{bmatrix} c_{xx} & c_{xy1} & c_{xy2} \\ c_{y1x} & c_{y1y1} & 0 \\ c_{y2x} & 0 & c_{y2y2} \end{bmatrix}, \boldsymbol{F} = \begin{bmatrix} F_d \sin(\omega_d t) \\ -2m_c\Omega_z\dot{x} \\ -2m_c\Omega_z\dot{x} \end{bmatrix}.$

are the mass, displacement, stiffness, damping and external force matrix, respectively; m_x is equivalent mass of drive mode; x is displacement of drive mode; y_1 and y_2 are displacements of sensing in-phase and anti-phase modes, respectively; Q_{y1} and Q_{y2} are quality factors; Ω_z is angular rate input; sensing mode mass m_y approximates to Coriolis mass m_c; F_d and ω_d are stimulating magnitude and frequency of drive mode; $c_{xx=}\omega_{x2}m_x/Q_{x2}$, $c_{y1y1=}\omega_{y1}m_y/Q_{y1}$, $c_{y2y2=}\omega_{y2}m_y/Q_{y2}$ and $k_{xx=}\omega_{x2}{}^2m_x$, $k_{y1y1=}\omega_{y1}{}^2m_y$, $k_{y2y2=}\omega_{y2}{}^2m_y$ are effective damping and stiffness of drive and sensing in-phase and anti-phase modes; c_{xy1}, c_{xy2} and c_{y1x}, c_{y2x} are coupling damping, k_{xy1}, k_{xy2} and k_{y1x}, k_{y2x} are coupling stiffness (caused by machining error) between drive and sensing in-phase and anti-phase modes, respectively; sensing mode displacement $y = y_1 + y_2$, and for ideal gyro structure model (ignoring the coupling stiffness and damping), we get [35]:

$$\begin{aligned} x(t) = & \frac{F_d/m_x}{\sqrt{\left(\omega_{x2}^2-\omega_d^2\right)^2+\omega_{x2}^2\omega_d^2/Q_{x2}^2}}\sin\left(\omega_d t+\varphi_{x2}\right) \\ & +\frac{F_d\omega_{x2}\omega_d/m_xQ_x}{\left(\omega_{x2}^2-\omega_d^2\right)^2+\omega_{x2}^2\omega_d^2/Q_{x2}^2}e^{-\frac{\omega_{x2}}{2Q_{x2}}t}\cos\left(\sqrt{1-1/4Q_{x2}^2}\omega_{x2}t\right) \\ & +\frac{F_d\omega_d\left(\omega_{x2}^2/Q_{x2}^2+\omega_d^2-\omega_{x2}^2\right)/m_x}{\omega_{x2}\sqrt{1-1/4Q_{x2}^2}\left[\left(\omega_{x2}^2-\omega_d^2\right)^2+\omega_{x2}^2\omega_d^2/Q_{x2}^2\right]}e^{-\frac{\omega_{x2}}{2Q_{x2}}t}\sin\left(\sqrt{1-1/4Q_{x2}^2}\omega_{x2}t\right) \end{aligned} \tag{2}$$

$$\begin{aligned} y_{1,2}(t) = & \frac{F_c}{\sqrt{\left(\omega_{y1,2}^2-\omega_d^2\right)^2+\omega_{y1,2}^2\omega_d^2/Q_{y1,2}^2}}\sin\left(\omega_d t+\varphi_{x2}+\frac{\pi}{2}+\varphi_{y1,2}\right)- \\ & \frac{F_c\left[\omega_{y1,2}\omega_d\sin\varphi_{x2}/Q_{y1,2}+\left(\omega_{y1,2}^2-\omega_d^2\right)\cos\varphi_{x2}\right]}{\left(\omega_{y1,2}^2-\omega_d^2\right)^2+\omega_{y1,2}^2\omega_d^2/Q_{y1,2}^2}e^{-\frac{\omega_{y1,2}}{2Q_{y1,2}}t}\cos\left(\sqrt{1-1/4Q_{y1,2}^2}\omega_{y1,2}t\right)+ \\ & \frac{F_c\left[\omega_{y1,2}\left(\omega_{y1,2}^2-3\omega_d^2\right)\cos\varphi_{x2}/\left(2Q_{y1,2}\right)+\omega_d\left(\omega_{y1,2}^2/\left(2Q_{y1,2}^2\right)+\omega_{y1,2}^2-\omega_d^2\right)\sin\varphi_{x2}\right]}{\omega_{y1,2}\sqrt{1-1/4Q_{y1,2}^2}\left[\left(\omega_{y1,2}^2-\omega_d^2\right)^2+\omega_{y1,2}^2\omega_d^2/Q_{y1,2}^2\right]} \\ & e^{-\frac{\omega_{y1,2}}{2Q_{y1,2}}t}\sin\left(\sqrt{1-1/4Q_{y1,2}^2}\omega_{y1,2}t\right) \end{aligned} \tag{3}$$

where $\varphi_{x2} = -tg^{-1}\left(\frac{\omega_{x2}\omega_d}{Q_{x2}\left(\omega_{x2}^2-\omega_d^2\right)}\right), F_c = \frac{-2\Omega_z\omega_dF_d}{m_x\sqrt{\left(\omega_{x2}^2-\omega_d^2\right)^2+\omega_{x2}^2\omega_d^2/Q_{x2}^2}}, \varphi_{y1,2} = -tg^{-1}\left(\frac{\omega_{y1,2}\omega_d}{Q_{y1,2}\left(\omega_{y1,2}^2-\omega_d^2\right)}\right).$

The abovementioned equations indicate that the movement of drive and sensing modes are the compound motion of stable vibration and attenuation vibration. Since drive mode closed loop

is employed, drive mode is stimulated with stable amplitude (ω_d = ω_{x2}). Then (2) can be simplified as [20]:

$$x(t) = \frac{F_d Q_{x2}}{m_x \omega_d^2} \cos(\omega_d t) = A_x \cos(\omega_d t) \tag{4}$$

The sensing in-phase and anti-phase modes movement equation can be got from (3):

$$y_{1,2}(t) = \frac{-2\Omega_z F_d Q_{x2} \sin(\omega_d t)}{m_x \omega_d \sqrt{\left(\omega_{y1,2}^2 - \omega_d^2\right)^2 + \omega_{y1,2}^2 \omega_d^2 / Q_{y1,2}^2}} = A_{y1,2} \sin(\omega_d t) \tag{5}$$

Then, the mechanical sensitivity can be expressed as:

$$S_{me} = \frac{A_{y1} + A_{y2}}{\Omega_z} \approx \frac{-F_d Q_x}{m_x \omega_d^2} \left(\frac{1}{\omega_{y1} - \omega_{x2}} + \frac{1}{\omega_{y2} - \omega_{x2}} \right) = -A_x \left(\frac{1}{\Delta\omega_1} + \frac{1}{\Delta\omega_2} \right) \tag{6}$$

The mechanical sensitivity of dual-mass sensing mode coupled structure is determined by vibration amplitude of drive mode and frequency differences between drive working mode and sensing modes (including the second and third modes). Furthermore, the one near the fourth mode is the dominant element. Therefore, the sensing anti-phase mode determines the gyro structure mechanical sensitivity. The schematic diagram of gyro sensing mode is shown in **Figure 4**. $G_{inphase}$ and $G_{anphase}$ are transform functions of in-phase and anti-phase sensing modes; K_{inyv} and K_{anyv} are displace-voltage transform parameters of sensing in-phase and anti-phase modes; K_{pre} is the preamplifier; V_{stotal} is sensing mode output and $G_{sV/F}$ can be expressed as:

$$G_{sV/F} = \left(G_{inphase} K_{inyv} + G_{anphase} K_{anyv} \right) K_{pre} \tag{7}$$

where $G_{inphase} = \frac{1}{m_y} \frac{1}{s^2 + \frac{\omega_{y1}}{Q_{y1}} s + \omega_{y1}^2}$ and $G_{anphase} = \frac{1}{m_y} \frac{1}{s^2 + \frac{\omega_{y2}}{Q_{y2}} s + \omega_{y2}^2}$ are the sensing in-phase and anti-phase mode transform functions, respectively.

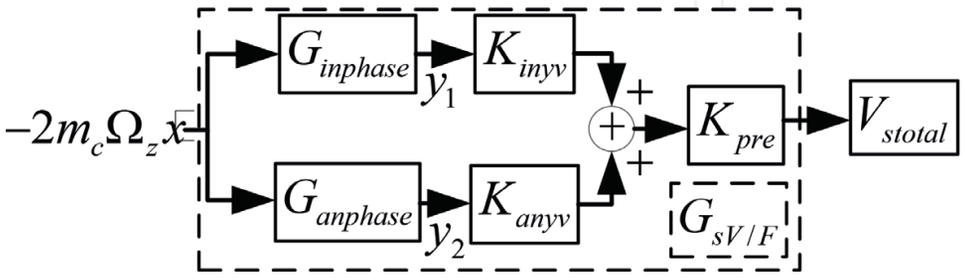

Figure 4. Schematic diagram of sensing mode real working mode.

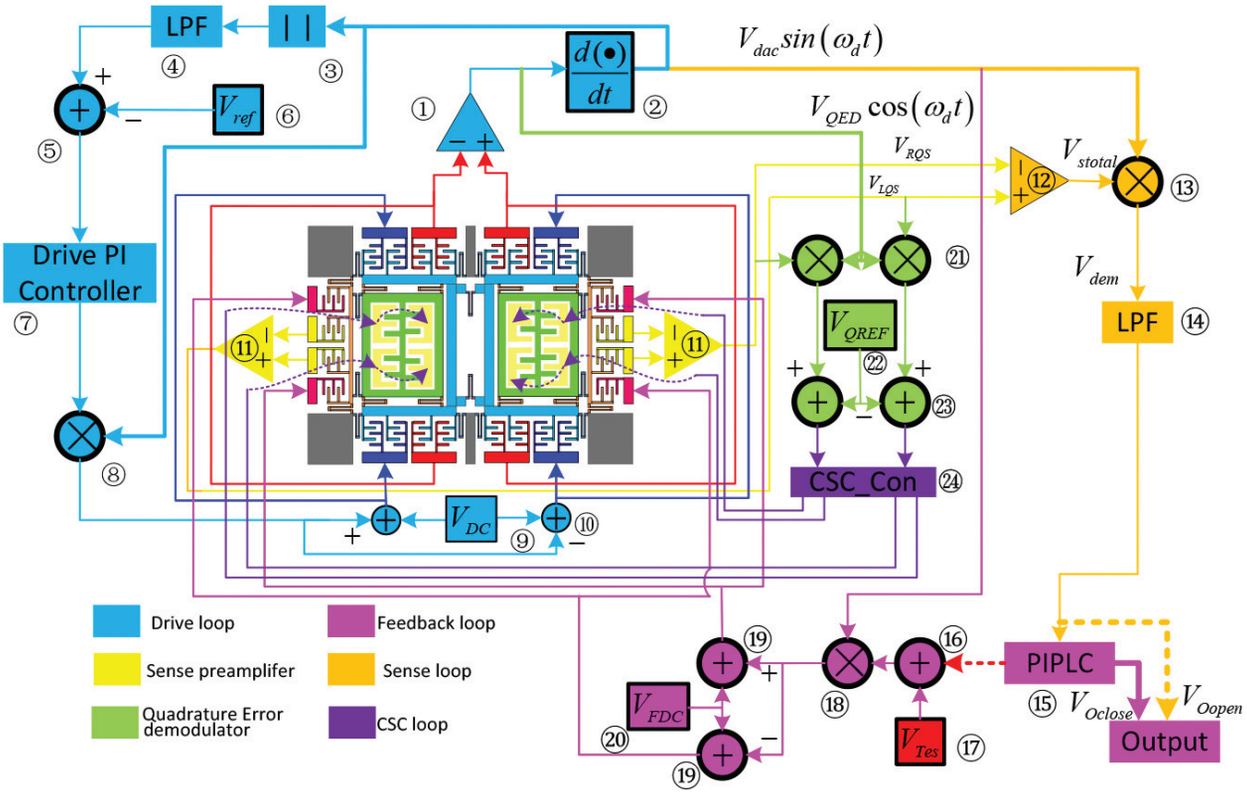

Figure 5. Dual-mass gyroscope monitoring system schematic.

2.3. Dual-mass MEMS gyroscope monitoring system

The gyro control and detection system is shown in **Figure 5**. In drive loop, the drive frame displacement $x(t)$ is detected by drive sensing combs and picked up by differential amplifier ①. Then, the signal phase is delayed by 90° (through ②) to satisfy the phase requirement of AC drive signal $V_{dac}Sin(\omega_d t)$. After that, $V_{dac}Sin(\omega_d t)$ is processed by a full-wave rectifier ③ and a low pass filter ④. Afterwards, V_{dac} is compared (in ⑤) with the reference voltage V_{ref} ⑥. Next, drive PI controller ⑦ generates the control signal, which is modulated by $V_{dac}Sin(\omega_d t)$, and then the signal is superposed (through ⑩) by V_{DC} ⑨ to stimulation drive mode. The sensing system employs a closed loop, which utilizes the same interface as drive circuit. First, the left and right masses' sensing signals are detected separately with differential detection amplifier⑪. And the output signals V_{RQS} (from right mass) and V_{LQS} (from left mass) are processed by second differential amplifier⑫ to generate signal V_{stotal}. Then, V_{stotal} is demodulated by signal $V_{dac}Sin(\omega_d t)$ (in ⑬). After that, the demodulated signal V_{dem} passes through the low pass filter ⑭; so, the sensing mode's movement signal V_{Oopen} can be got. For sense closed loop ("pink" section in **Figure 5**), V_{Oopen} is first sent in proportional-integral-phase-leading controller (PIPLC) ⑮ to calculate the control signal superposed (through ⑯) with test signal V_{Tes} ⑰. Then the signal is modulated with $V_{dac}Sin(\omega_d t)$ (in ⑱). Finally, DC voltage V_{FDC} ⑳ is superposed with the modulated signal in ⑲ to generate the feedback signal. In quadrature error compensation system, V_{RQS} and V_{LQS} are demodulated by drive frame displacement signal $V_{QED}Cos(\omega_d t)$ separately in ㉑. The quadrature

error compensation reference is provided in ㉒ and is compared with quadrature error amplitude in ㉓; the results are sent to coupling stiffness compensation (CSC) controller ㉔.

3. Dual-mass MEMS gyroscope quadrature error compensation

3.1. Dual-mass MEMS gyroscope structure quadrature error model

The quadrature error is caused by coupling stiffness, which is generated in structure processing stage, and the stiffness elements in Eq. (1) can be calculated by:

$$\begin{cases} k_{xx} = k_x \cos^2\beta_{Qx} + k_y \sin^2\beta_{Qy} \\ k_{xy} = k_{yx} = k_x \sin\beta_{Qx} \cos\beta_{Qx} - k_y \cos\beta_{Qy} \sin\beta_{Qy} \\ k_{yy} = k_x \sin^2\beta_{Qx} + k_y \cos^2\beta_{Qy} \end{cases} \tag{8}$$

where k_x and k_y are the design stiffness along designed axis x and y; β_{Qx} and β_{Qy} are the quadrature error angle and they are the angles between practical axis and designed axis [11, 35], and usually it is assumed that $\beta_{Qx} = \beta_{Qy}$.

The equivalent stiffness and masses system and structure motion of dual-mass gyro structure is shown in **Figure 6**. The design drive and sense stiffness axis are x and y (gray); the real drive and sense axis of left and right masses after manufacture are x_l', x_r' (with light blue) and y_l', y_r' (with light yellow), respectively; the stiffness of drive and sense modes of left and right masses after manufacture are k_{lx}, k_{rx} (with dark blue) and k_{ly}, k_{ry} (with dark yellow), respectively; the projections of k_{lx} on $-x$- and y-axis are k_{lxx} and k_{lxy}; the projections of k_{rx} on x- and y-axis are k_{rxx} and k_{rxy}; the projections of k_{ly} on $-x$- and y-axis are k_{lyx} and k_{lyy}; the projections of k_{ry} on x- and y-axis are k_{ryx} and k_{ryy}; the quadrature error angular of left and right masses are β_{ly} and β_{ry}. In design stage, $|k_{lx}| = |k_{rx}|$, $|k_{ly}| = |k_{ry}|$, and $\beta_{ly} = \beta_{ry} = 0$, but after the manufacture process, the parameters change and they do not meet the equal equations, so the coupling stiffness of two masses are different.

3.2. Dual-mass MEMS gyroscope structure coupling stiffness compensation

The CSC method utilizes quadrature error correction combs to generate negative electrostatic stiffness and correct quadrature error coupling stiffness. This special comb is unequal gap style, and is introduced in [11]; its stiffness is expressed as:

$$k_{qxy} = k_{qyx} = k_{qcoup} V_{qD} V_{qc} = -\frac{4 n_q \varepsilon_0 h}{{y_{q0}}^2} \left(1 - \frac{1}{\lambda^2}\right) V_{qD} V_{qc} \tag{9}$$

where k_{qxy} and k_{qyx} are the quadrature error correction comb stiffness along designed axes x and y; V_{qD} and V_{qc} are correction fixed voltage and controlling voltage; n_q is the number of comb; ε_0 is the permittivity of vacuum; h is the thickness of the comb; y_{q0} and x_0 are the parallel capacitance's gap and overlap length, respectively; λ is a constant. **Figure 7** shows the right mass CSC system which is same with left mass CSC system, $G_{RsV/F}$ is the transform function of

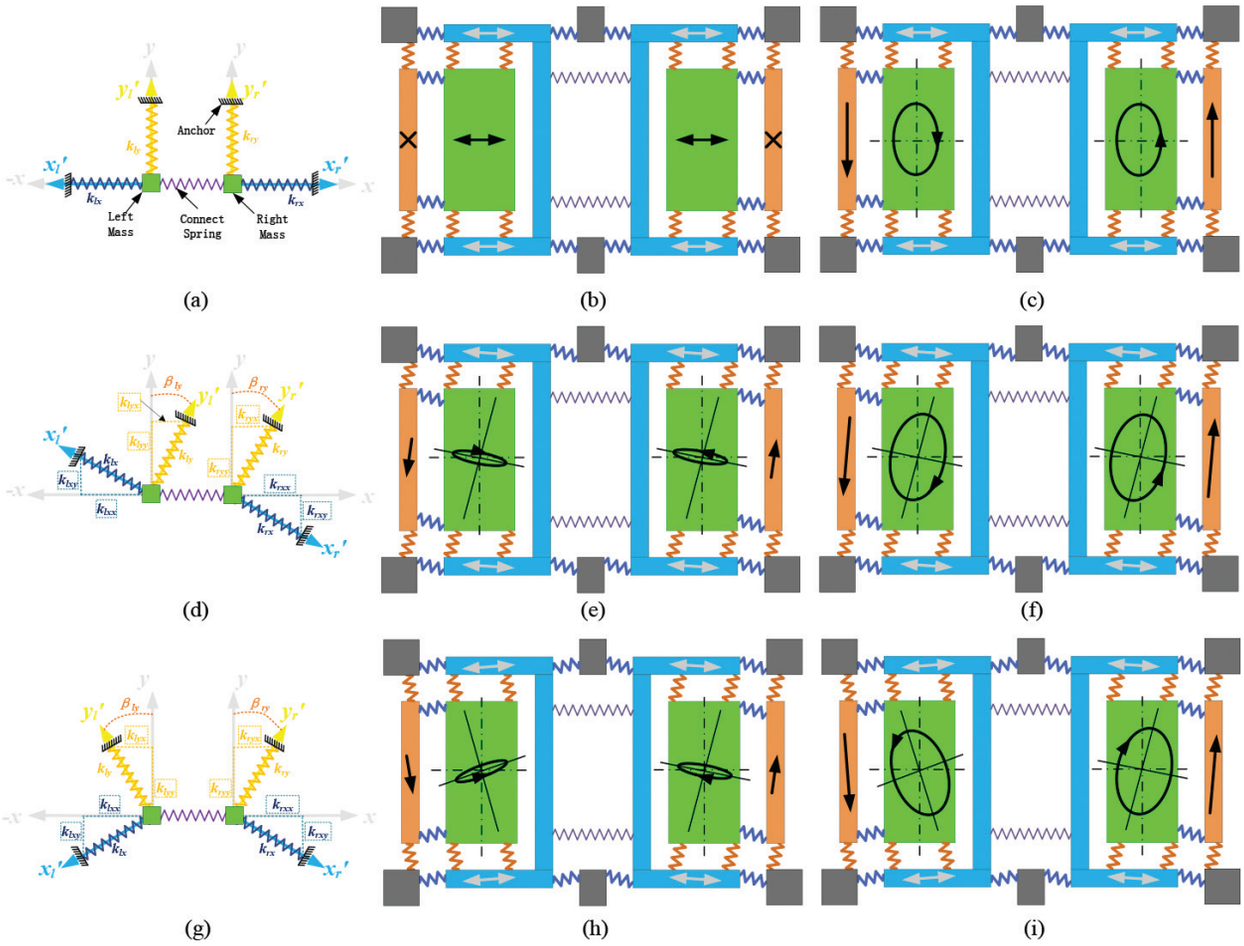

Figure 6. (a) Stiffness system of ideal dual-mass gyro structure; (b) ideal structure movement without angular rate input; (c) ideal structure movement with steady angular rate input; (d) stiffness system with in-phase quadrature error angular; (e) the movement of in-phase quadrature error angular structure without angular rate input; (f) the movement of in-phase quadrature error angular structure with steady angular rate input; (g) stiffness system with anti-phase quadrature error angular; (h) the movement of anti-phase quadrature error angular structure without angular rate input; (i) the movement of anti-phase quadrature error angular structure with steady angular rate input.

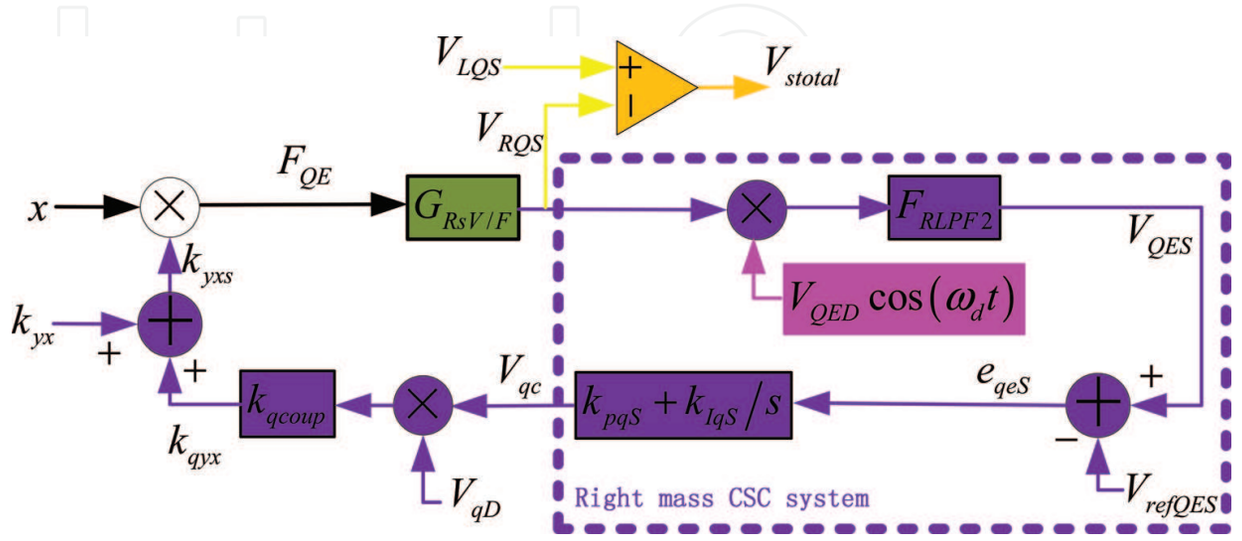

Figure 7. Right mass SCS system.

right mass. In **Figure 7**, the coupling stiffness k_{yx} is modulated by drive-mode movement, and the controller employs PI controlling technology. The correction stiffness does not need to be modulated by quadrature error in-phase signal, which is better for circuit simplification and power consumption. We can get the following equations:

$$V_{RQS} = F_{QE}G_{RsV/F} = x\left(k_{yx} + k_{qyx}\right)G_{RsV/F} \tag{10}$$

$$V_{qc} = \left(V_{QES} - V_{refQES}\right)\left(k_{pqS} + \frac{k_{IqS}}{s}\right) \tag{11}$$

We have $x = A_x cos(\omega_d t)$ and $V_{refQES} = 0$, after the low pass filter, V_{QES} can be expressed as:

$$V_{QES} = \frac{1}{2}A_x\left(k_{yx} + k_{qyx}\right)G_{RsV/F}V_{QED} \tag{12}$$

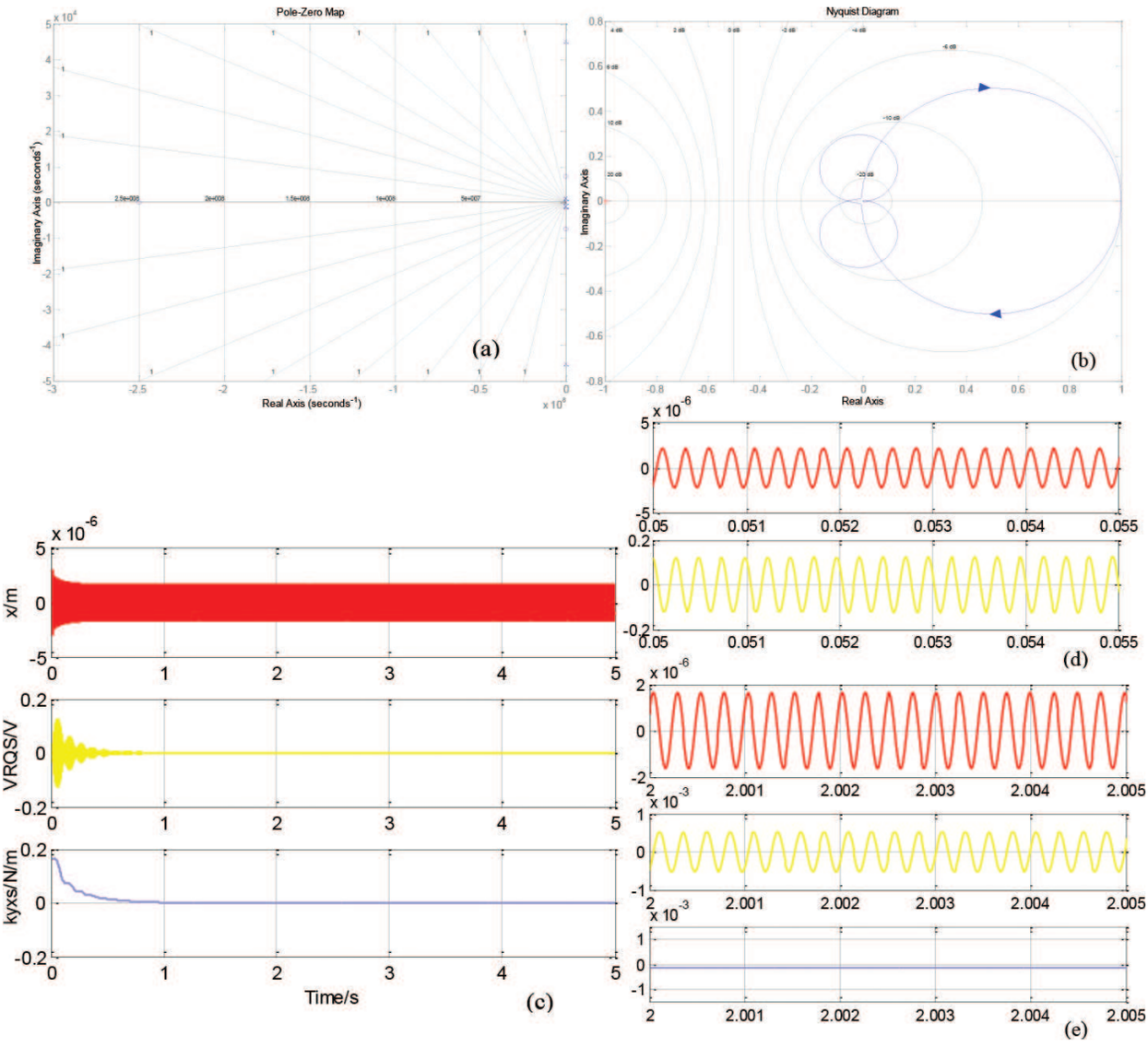

Figure 8. (a) CSC system pole-zero map; (b) CSC system Nyquist diagram; (c) CSC system simulation curves; (d) CSC system start-up stage enlarge curves; (e) CSC system stable stage enlarge curves.

Then, combining (9), (11) and (12), we have:

$$\frac{k_{qyx}(s)}{k_{yx}(s)} = \frac{\frac{A_x}{2}k_{qcoup}V_{qD}V_{QED}F_{RLPF2}(s)\left[G_{RsV/F}(s+j\omega_d)+G_{RsV/F}(s-j\omega_d)\right]\left(k_{pqS}+\frac{k_{IqS}}{s}\right)}{1-\frac{A_x}{2}k_{qcoup}V_{qD}V_{QED}F_{RLPF2}(s)\left[G_{RsV/F}(s+j\omega_d)+G_{RsV/F}(s-j\omega_d)\right]\left(k_{pqS}+\frac{k_{IqS}}{s}\right)} \quad (13)$$

When the system is under stable state, s = 0, and the above equation has:

$$1 = \frac{A_x}{2}k_{qcoup}V_{qD}V_{QED}F_{LPF2}(s)\left[G_{RsV/F}(s+j\omega_d)+G_{RsV/F}(s-j\omega_d)\right]\left(k_{pqS}+\frac{k_{IqS}}{s}\right)\Big|_{s=0} \quad (14)$$

Then:

$$k_{qyx} \approx -k_{yx} \quad (15)$$

The coupling stiffness is corrected. The CSC system is simulated and the curves are shown in **Figure 8**. The Pole-Zero Map is shown in **Figure 8(a)**, no pole is in the positive real axis and **Figure 8(b)** is the Nyquist Diagram, the curve does not contain (−1,0j) point, which proves the system's stability. The time-domain simulation curves are shown in **Figure 8(c)–(e)**, and the curves indicate that the CSC system is under stable state after about 0.7 s. It is obvious that in start-up stage, the sense channel signal mainly consists of quadrature error signal. But, in stable state, the dominate element is Coriolis in-phase signal. Furthermore, the overall coupling stiffness k_{yxs} is suppressed from original value (about 0.18 N/m) to −0.00016 N/m, and k_{yx} is basically corrected which proves (15).

4. Dual-mass MEMS gyroscope bandwidth expansion

4.1. Dual-mass MEMS gyroscope structure sense mode model

The force rebalancing combs stimulation method (FRCSM) is employed to test the sense mode. Force rebalancing combs are slide-film form (does not vary ω_{y1} and ω_{y2}). And they are arranged to generate electrostatic force and rebalance the Coriolis force applied on sense frame. The movement of sensing frame is restricted, which improves the dynamic performance of gyro. Therefore, Coriolis simulation signal is designed to be produced through force rebalancing combs, and this method can be further applied to scale factor and bandwidth tests. The FRCSM schematic diagram is shown in **Figure 9**, and the equivalent input angular rate of V_{Tes} is:

$$\Omega_{VTes} = \frac{K_{FBy}V_{Tes}V_{dac}}{2m_cA_x\omega_d} \quad (16)$$

where K_{FBy} is voltage-force interface transform coefficient of force rebalances combs; V_{dac} is modulate signal amplitude, which is picked up after 90° shifter in drive loop and is considered to be constant when gyro works. K_{FBy} can be got either from the calculation of structure parameter or turntable test, and it is determined by force rebalancing combs number,

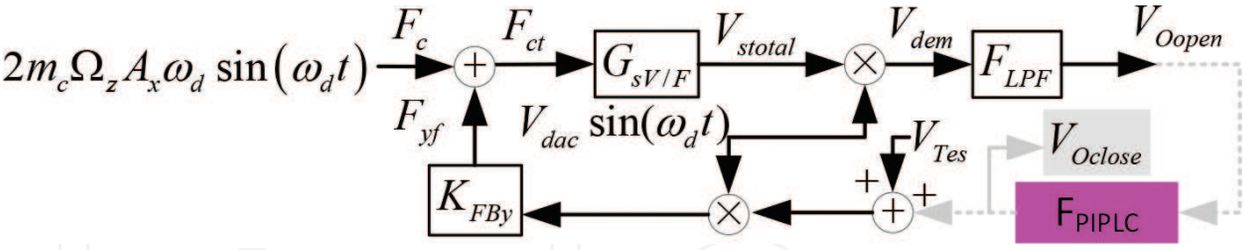

Figure 9. FRCSM schematic in sensing loop.

parameters and feedback direct voltage V_{FDC}. The system diagram of sense open loop is shown in **Figure 9**, and the equations below can be derived from **Figure 9**:

$$\begin{cases} F_{ct}(t) = 2\Omega_z(t)m_y A_x\omega_d \sin(\omega_d t) + K_{FBy}V_{Tes}(t)V_{dac}\sin(\omega_d t) \\ V_{Oopen} = F_{ct}(t)G_{sV/F}V_{dac}\sin(\omega_d t)F_{LPF} \end{cases} \tag{17}$$

After Laplace transformation, we can get [35]:

$$V_{Oopen}(s) = K_{pre}\left[\frac{A_x\omega_d V_{dac}\Omega_z(s)F_{LPF}(s)}{2} + \frac{K_{FBy}V_{dac}^2 V_{Tes}(s)F_{LPF}(s)}{4m_y}\right]G_{sV/F}(s) \tag{18}$$

where, $G_{sV/F}(s) = \left[\frac{K_{inyv}\left(s^2+\frac{\omega_{y1}}{Q_{y1}}s+\omega_{y1}^2-\omega_d^2\right)}{\left(s^2+\frac{\omega_{y1}}{Q_{y1}}s+\omega_{y1}^2-\omega_d^2\right)^2+\left(2s\omega_d+\frac{\omega_{y1}}{Q_{y1}}\omega_d\right)^2} + \frac{K_{anyv}\left(s^2+\frac{\omega_{y2}}{Q_{y2}}s+\omega_{y2}^2-\omega_d^2\right)}{\left(s^2+\frac{\omega_{y2}}{Q_{y2}}s+\omega_{y2}^2-\omega_d^2\right)^2+\left(2s\omega_d+\frac{\omega_{y2}}{Q_{y2}}\omega_d\right)^2}\right]$, and ω_d = 3488.9*2π rad/s, ω_{y1} = 3360.1*2π rad/s, ω_{y2} = 3464.1*2π rad/s, Q_{y1} = 1051 and Q_{y2} = 1224, then the Bode Diagram map is shown in **Figure 10**, and the bandwidth of the mechanical system is [20, 35]:

$$\omega_b = 0.54\Delta\omega_2 \tag{19}$$

In **Figure 10**, point A (frequency is $\Delta\omega_2$) and C (frequency is $\Delta\omega_1$) peak points are generated by two conjugate poles, respectively; B valley point ($\Delta\omega_B$) is caused by conjugate zeros shown in Eq. (18). The bandwidth obtained from the simulation curve is 12.9 Hz and from FRCSM test curve is 13 Hz, which verifies the theory calculation result in Eq. (19). In addition, the FRCSM test curve matches simulation curve well and proves the theory analysis conclusion proposed in Section 2.2.

4.2. Dual-mass MEMS gyroscope bandwidth expanding

Sensing closed-loop control method provides electrostatic force to rebalance the Coriolis force applied on sensing mode, which is one of the most effective ways to improve gyro dynamic performance. When sensing closed-loop works, the sensing frame's displacement is restricted and the Coriolis force is transformed into electronic signal directly. And it also avoids the nonlinearity of sensing mode displacement. Meanwhile, closed loop provides better anti-vibration and anti-shock characteristics to the gyroscope. The sensing closed-loop schematic is shown in **Figure 9**, where the real input angular rate Ω_z = 0°/s and the simulation angular

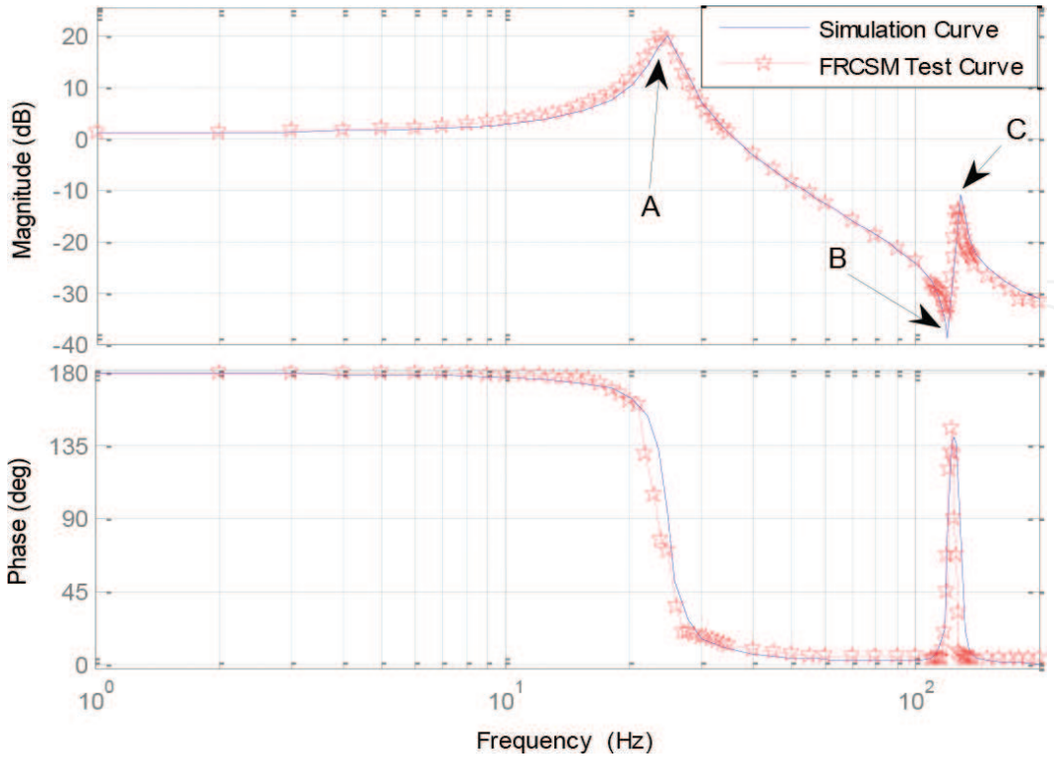

Figure 10. Simulation and FRCSM test results of dual-mass gyroscope structure bode diagram.

rate V_{Tes} is employed to test the closed system frequency response. From **Figure 8**, the equations can be derived:

$$F_{yf}(t) = K_{FBy}[V_{Oclose}(t) + V_{Tes}(t)]V_{dac}\sin(\omega_d t) \tag{20}$$

$$V_{Oclose}(s) = V_{dem}(s)F_{LPF}(s)F_{PIPLC}(s) \tag{21}$$

Combining Eq. (20) with (21), we have:

$$\left|\frac{V_{Oclose}(\omega_{open})}{\Omega_{VTes}(\omega_{open})}\right| = \frac{2m_c A_x \omega_d K_{pre} G_{se} V_{dac} F_{LPF}(s) F_{PIPLC}(s)}{4m_y - K_{pre}K_{FBy}V_{dac}^2 G_{se} F_{LPF}(s)F_{PIPLC}(s)} \tag{22}$$

Because $4m_y \ll K_{pre}K_{FBy}V_{dac}^2 G_{se}F_{LPF}(s)F_{PIPLC}(s)$within bandwidth range ($G_{se}$ reduces a lot at point B, so bandwidth range is considered before point B), Eq. (22) can be expressed as:

$$\left|\frac{V_{Oclose}}{\Omega_{VTes}}\right| = \frac{2m_c A_x \omega_d}{K_{FBy}V_{dac}} \tag{23}$$

The above equation means that the scale factor in closed loop is constant value and is not restricted by resonant peak (A point).

Generally speaking, the open-loop Bode diagram of sensing closed-loop is expected to have the following characteristics: (a) In low frequency range, a first-order pure integral element is configured to achieve enough gain and reduce the steady state error of the system, (b) In

middle frequency range, the slope of magnitude line is designed to be −20 dB/dec at 0 dB crossing frequency point. The cut off frequency is ω_{cut}, which provides enough phase margin (more than 30°), (c) At $\Delta\omega_2$ frequency point (A point), the phase lags 180° acutely, so two first-order differential elements are utilized to compensate the system phase before $\Delta\omega_2$. After the phase compensation, the −180° crossing frequency is improved and optimizes the magnitude margin (expected more than 5 dB), (d) Since a pair of conjugate zero is at $\Delta\omega_B$, which provides +20 dB/dec magnitude curve, cut off frequency ω_{cut} is arranged before $\Delta\omega_B$, (e) In high frequency range, the magnitude curve is designed to be −60 dB/dec to reduce magnitude rapidly, which restrains high frequency noise and white noise effectively. F_{LPF} element is second-order type and generates −40 dB/dec, and a pair of conjugate pole is at $\Delta\omega_1$, providing −20 dB/dec slope, (f) An inertial element is required to match the phase compensation elements and its frequency should be arranged outside the bandwidth. Meanwhile, the inertial element also provides another −20 dB/dec slope in high frequency range, which is better to restrain high frequency noise and (g) Temperature compensation module is required to ensure the wide-temperature range characteristic of PIPLC. So, the PIPLC is expressed as:

$$F_{PIPLC}(s) = k_{pi}(t_{tem})\frac{s+\omega_{pi1}}{s}\frac{s+\omega_{pi1}}{s+\omega_{pi2}(t_{tem})} \tag{24}$$

According to the analysis, we make k_{pi} = 32 (experience value, over high value brings instability), ω_{pi1} = 10π rad/s and ω_{pi2} = 400π rad/s. In addition, the k_{pi} and ω_{pi2} can be adjusted by temperature t_{tem}. The PIPLC circuit diagram is shown in **Figure 11**. The transform function can be written as following:

The open-loop Bode Diagram of the sensing closed-loop is simulated in Simulink software and shown in **Figure 12(a)**. **Figure 12** indicates that the minimum phase margin of the loop is 34.6° and the magnitude margin is 7.21 dB, which satisfy the design requests. The Pole-Zero Map and Nyquist Map of sensing closed-loop are shown in **Figure 12(b)** and **(c)**. The poles distribute in negative side of real axis and the Nyquist curve does not contain (−1, 0j) point. These two criterions both illustrate the closed system is pretty stable. The Bode Diagram of sensing closed-loop simulation is shown in **Figure 12(d)**, whose curves indicate that the bandwidth of the gyro is 100 Hz, the lowest point within the bandwidth range is −13.8 dB, the DC magnitude is −12.3 dB and the highest point is −10.4 dB. The resonant peak point A (shown in **Figure 10**) is compensated, and the new bandwidth bottleneck point is valley B. Therefore, one of the best methods to expand the bandwidth under this condition is to enlarge the frequency

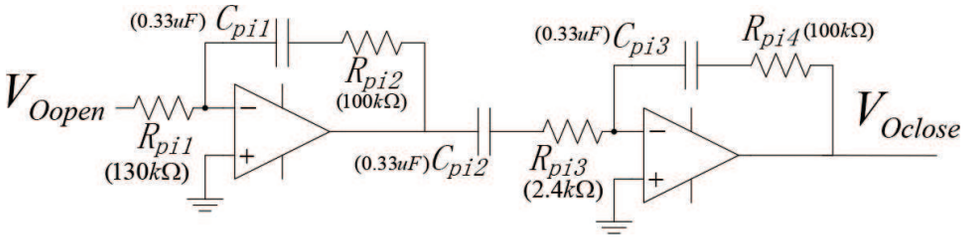

Figure 11. PIPLC circuit diagram.

http://dx.doi.org/10.5772/intechopen.74364

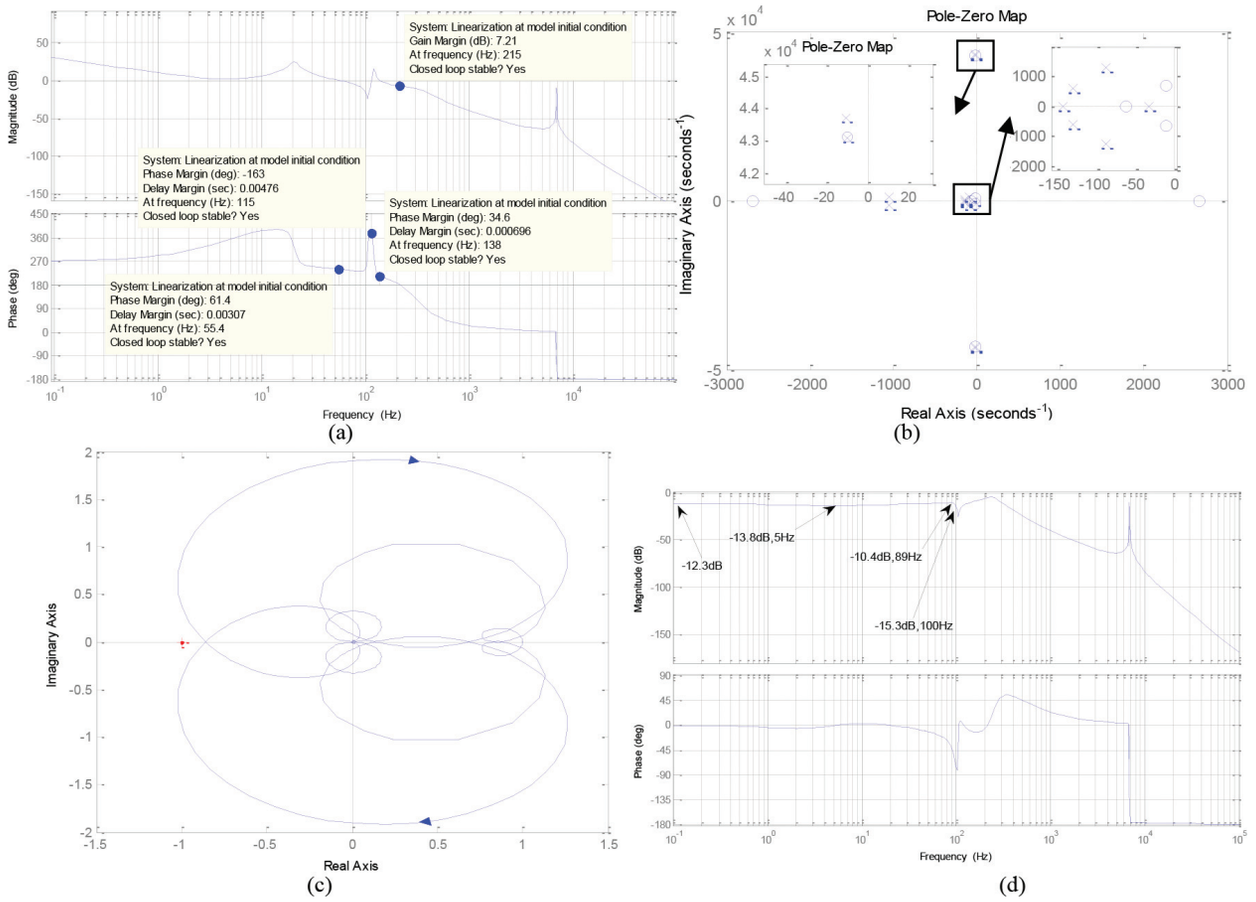

Figure 12. (a) Open-loop bode diagram of sensing close loop; (b) pole-zero map of sensing close loop; (c) Nyquist map of sense close loop; (d) sense close loop simulation bode diagram.

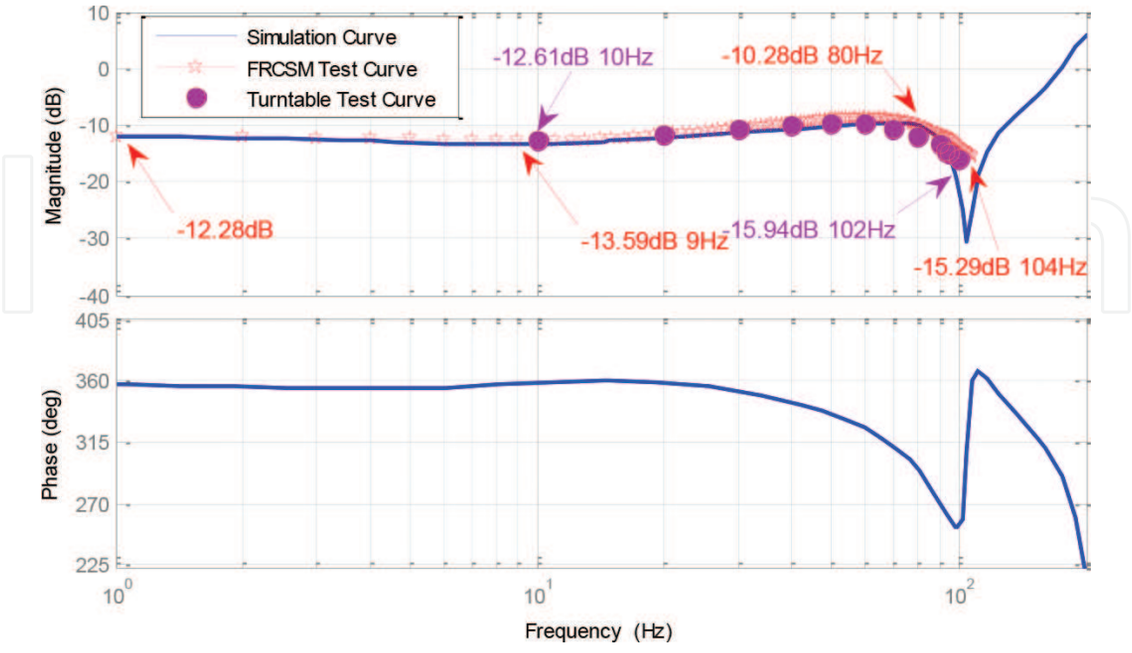

Figure 13. Dual-mass gyroscope bandwidth test.

difference between ω_{y1} and ω_{y2}. The gyro is fixed on the turntable and tested under room temperature (about 20°C) with FRCSM. More specifically, the employed method is a step-by-step test and step length is 1 Hz. First, the result is shown as **Figure 13** with red stars, where the bandwidth is about 104 Hz (as the simulation value is 102 Hz in **Figure 13**) [23]. Since the scale factor can be adjusted with the output level amplifier, the −3 dB point is the key, not the absolute value of the magnitude. After the turntable test is done, since the turntable's swing frequency value is hard to get accurately, we mainly focus on the bandwidth, not each frequency point's value. Within the bandwidth range, the step-by-step test (step length is 10 Hz) is carried out, and the bandwidth is found to be 102 Hz, which verifies the FRCSM result.

5. Conclusion

In this chapter, the recent achievements in our research group for dual-mass MEMS gyroscope are proposed. Three main parts are discussed: dual-mass gyroscope structure design, quadrature error electrostatic compensation and bandwidth expansion. First, dual-mass MEMS gyroscope structure is designed and simulated in ANSYS soft and dual-mass structure movement function is derived. Second, quadrature error is traced to the source, and the coupling stiffness electrostatic compensation method is employed to reduce the quadrature error. Finally, proportional-integral-phase-leading controller is presented in sensing close loop to expand the bandwidth from 13 to 104 Hz.

Acknowledgements

This work was supported by National Natural Science Foundation of China No.51705477. The research was also supported by Research Project Supported by Shanxi Scholarship Council of China No. 2016-083, Fund of North University of China, Science and Technology on Electronic Test and Measurement Laboratory No. ZDSYSJ2015004, and The Open Fund of State Key Laboratory of Deep Buried Target Damage No. DXMBJJ2017-15. The authors deliver their special gratitude to Prof. Hongsheng Li (Southeast University, Nanjing, China) and his group for the guidance, discussions and help.

Author details

Huiliang Cao[1]* and Jianhua Li[2]

*Address all correspondence to: caohuiliang1986@126.com

1 Science and Technology on Electronic Test and Measurement Laboratory, North University of China, Tai Yuan, China

2 National Key Laboratory of Science and Technology on Electromechanical Dynamic Control, Beijing Institute of Technology, Beijing, China

References

[1] Zaman M, Sharma A, Hao Z, et al. A mode-matched silicon-yaw tuning-fork gyroscope with subdegree-per-hour Allan deviation bias instability. Journal of Microelectromechanical Systems. 2008;(6):1526-1536. DOI: 10.1109/jmems.2008.2004794

[2] Xu Y, Chen XY, Wang Y. Two-mode navigation method for low-cost inertial measurement unit-based indoor pedestrian navigation. Journal of Chemical Information & Computer Sciences. 2016;**44**(5):1840-1848. DOI: 10.1177/0037549716655220

[3] Huang H, Chen X, Zhang B, et al. High accuracy navigation information estimation for inertial system using the multi-model EKF fusing Adams explicit formula applied to underwater gliders. ISA TRANSACTIONS. 2017;**66**:414-424. DOI: 10.1016/j.isatra.2016.10.020

[4] Antonello R, Oboe R. Exploring the potential of MEMS gyroscopes. IEEE Industrial Electronics Magazine. 2012;**3**:14-24. DOI: 10.1109/mie.2012.2182832

[5] Xia DZ, Yu C, Kong L. The development of micromachined gyroscope structure and circuitry technology. Sensors. 2014;**14**:1394-1473. DOI: 10.3390/s140101394

[6] Cao HL, Li HS. Investigation of a vacuum packaged MEMS gyroscope structure's temperature robustness. International Journal of Applied Electromagnetics & Mechanics. 2013;**4**: 495-506. DOI: 10.3233/jae-131668

[7] Tatar E, Alper S, Akin T. Quadrature- error compensation and corresponding effects on the performance of fully decoupled MEMS gyroscopes. Journal of Microelectromechanical Systems. 2012;(3):656-667. DOI: 10.1109/jmems.2012.2189356

[8] Chaumet B, Leverrier B, Rougeot C, et al. A new silicon tuning fork gyroscope for aerospace applications. In: Proceedings of Symposium Gyro Technology. 2009, 1.1-1.13

[9] Saukski M, Aaltonen L, Halonen K. Zero-rate output and quadrature compensation in vibratory MEMS gyroscopes. IEEE Sensors Journal. 2007;(12):1639-1652. DOI: 10.1109/jsen.2007.908921

[10] Tally C, Waters R, Swanson P. Simulation of a MEMS Coriolis gyroscope with closed-loop control for arbitrary inertial force, angular rate, and quadrature inputs. Proceedings of IEEE Sensors. 2011:1681-1684

[11] Li HS, Cao HL, Ni YF. Electrostatic stiffness correction for quadrature error in decoupled dual-mass MEMS gyroscope. Journal of Micro-Nanolithography Mems And Moems. 2014;**13**(3): 033003. DOI: 10.1117/1.jmm.13.3.033003

[12] Walther A, Blanc CL, Delorme N, Deimerly Y, Anciant R, Willemin J. Bias contributions in a MEMS tuning fork gyroscope. Journal of Microelectromechanical Systems. 2013;**22**(2): 303-308. DOI: 10.1109/jmems.2012.2221158

[13] Cao HL, Li HS, Liu J et al. An improved interface and noise analysis of a turning fork microgyroscope structure. Mechanical Systems and Signal Processing. 2016;**s 70–71**:1209-1220. DOI: 10.1016/j.ymssp.2015.08.002

[14] Su J, Xiao D, Wu X, et al. Improvement of bias stability for a micromachined gyroscope based on dynamic electrical balancing of coupling stiffness. Journal of Micro-Nanolithography Mems And Moems. 2013;**12**(3):033008. DOI: 10.1117/1.jmm.12.3.033008

[15] Ni YF, Li HS, Huang LB. Design and application of quadrature compensation patterns in bulk silicon micro-gyroscopes. Sensors. 2014;**14**:20419-20438. DOI: 10.3390/s141120419

[16] Seeger J, Rastegar A, Tormey T. Method and apparatus for electronic cancellation of quadrature error : United States Patent. No. 7290435B2; 2007

[17] Maurer M, Northemann T, Manoli Y. Quadrature compensation for gyroscopes in electro-mechanical bandpass ΣΔ-modulators beyond full-scale limits using pattern recognition. Procedia Engineering. 2011;**25**:1589-1592. DOI: 10.1016/j.proeng.2011.12.393

[18] Antonello R, Oboe R, Prandi L, et al. Open loop compensation of the quadrature error in MEMS vibrating gyroscopes. In: Proceedings of the IEEE Industrial Electronics Society Conference; 2009. pp. 4034-4039

[19] Cao HL, Li HS, Sheng X, et al. A novel temperature compensation method for a MEMS gyroscope oriented on a periphery circuit. International Journal of Advanced Robotic System. 2013;**10**(5):1-10. DOI: 10.5772/56759

[20] M H Bao. Handbook of sensors and actuators. 1st ed. Amsterdam; The Netherlands, Elsevier; 2000. DOI: 10.1016/9780444505583

[21] Ezekwe CD, Boser BE. A mode-matching ΣΔ closed-loop vibratory gyroscope readout interface with a 0.004°/s/√Hz noise floor over a 50Hz band. IEEE Journal of Solid-State Circuits. 2008;**43**(12):3039-3048. DOI: 10.1109/jssc.2008.2006465

[22] Sonmezoglu S, Alper SE, Akin T. An automatically mode-matched MEMS gyroscope with wide and tunable bandwidth. Journal of Microelectromechanical Systems. 2014;**23**(2): 284-297. DOI: 10.1109/jmems.2014.2299234

[23] Sung WT, Sung S, Lee JG, Kang T. Design and performance test of a MEMS vibratory gyroscope with a novel AGC force rebalance control. Journal of Micromechanics & Microengineering. 2007;**17**(10):1939. DOI: 10.1088/0960-1317/17/10/003

[24] Cui J, Guo Z, Zhao Q, et al. Force rebalance controller synthesis for a micromachined vibratory gyroscope based on sensitivity margin specifications. Journal of Microelectro-mechanical. 2011;**20**(6):1382-1394. DOI: 10.1109/jmems.2011.2167663

[25] He C, Zhao Q, Liu Y, et al. Closed loop control design for the sensing mode of micromachined vibratory gyroscope. Science China-Technological Sciences. 2013;**56**(5): 1112-1118. DOI: 10.1007/s11431-013-5201-x

[26] Alshehri A, Kraft M, Gardonio P. Two-mass MEMS velocity sensor: Internal feedback loop design. IEEE Sensors Journal. 2013;**13**(3):1003-1011. DOI: 10.1109/jsen.2012.2228849

[27] Trusov AA, Schofield AR, Shkel AM. Study of substrate energy dissipation mechanism in in-phase and anti-phase micromachined vibratory gyroscope. In: IEEE Sensors Conference; 2008. pp. 168-171

[28] Y Ni, H Li, L Huang, et al. On bandwidth characteristics of tuning fork micro-gyroscope with mechanically coupled sensing mode. Sensors 2014;**14**(7):13024-13045. DOI: 10.3390/s140713024

[29] Si C, Han G, Ning J, Yang F. Bandwidth optimization design of a multi degree of freedom MEMS gyroscope. Sensors. 2013;**13**(8):10550-10560. DOI: 10.3390/s130810550

[30] Acar C, Shkel AM. An approach for increasing drive-mode bandwidth of MEMS vibratory gyroscopes. Journal of Microelectromechanical Systems. 2005;**14**(3):520-528. DOI: 10.1109/jmems.2005.844801

[31] Feng ZC, Fan M, Chellaboina V. Adaptive input estimation methods for improving the bandwidth of microgyroscopes. IEEE Sensors Journal. 2007;**7**(4):562-567. DOI: 10.1109/jsen.2007.891992

[32] Cui J, He C, Yang Z, et al. Virtual rate-table method for characterization of microgyroscopes. IEEE Sensors Journal. 2012;**12**(6):2192-2198. DOI: 10.1109/jsen.2012.2185489

[33] Y Yin, S Wang, C Wang, et al. Structure-decoupled dual-mass MEMS gyroscope with self-adaptive closed-loop. In: Proceedings of the 2010 5th IEEE International Conference on Nano/Micro Engineered and Molecular Systems; Xiamen. China: 2010. p. 624-627

[34] Cao HL, Li HS, Shao XL, Liu ZY, Kou ZW, Shan YH, Shi YB, Shen C, Liu J. Sensing mode coupling analysis for dual-mass MEMS gyroscope and bandwidth expansion within wide-temperature range. Mechanical Systems & Signal Processing. 2018;**98**:448-464. DOI: 10.1016/j.ymssp.2017.05.003

[35] Cao HL, Li HS, Kou ZW, Shi YB, Tang J, Ma ZM, Shen C, Liu J. Optimization and experiment of dual-mass MEMS gyroscope quadrature error correction methods. Sensors. 2016;**16**(1):71. DOI: 10.3390/s16010071

IntechOpen